



A Cavity-Enhanced UV Absorption Instrument for High Precision, Fast Time Response Ozone Measurements

Reem A. Hannun^{1,2}, Andrew K. Swanson^{1,3}, Steven A. Bailey¹, Thomas F. Hanisco¹, T. Paul Bui⁴, Ilann Bourgeois^{5,6}, Jeff Peischl^{5,6}, Thomas B. Ryerson⁵

- 5 ¹Atmospheric Chemistry and Dynamics Laboratory, NASA Goddard Spaceflight Center, Greenbelt, MD, USA
²Joint Center for Earth Systems Technology, University of Maryland Baltimore County, Baltimore, MD, USA
³Universities Space Research Association, Columbia, MD, USA
⁴Earth Science Division, NASA Ames Research Center, Moffett Field, CA, USA
⁵NOAA Chemical Sciences Laboratory, Boulder, CO, USA
10 ⁶Cooperative Institute for Research in Environmental Sciences, University of Colorado Boulder, Boulder, CO, USA

Correspondence to: Reem A. Hannun (reem.a.hannun@nasa.gov)

Abstract. The NASA Rapid Ozone Experiment (ROZE) is a broadband cavity-enhanced UV absorption instrument for the detection of *in situ* ozone (O₃). ROZE uses an incoherent LED light source coupled to a high-finesse optical cavity to achieve an effective pathlength of ~104 m. Due to its high-sensitivity and small optical cell volume, ROZE demonstrates a 1 σ precision of 80 pptv (0.1 s) and 31 pptv (1 s), as well as a 1/e response time of 50 ms. ROZE can be operated in a range of field environments, including low- and high-altitude research aircraft, and is particularly suited to O₃ vertical flux measurements using the eddy covariance technique. ROZE was successfully integrated aboard the NASA DC-8 aircraft during July–September 2019 and validated against a well-established chemiluminescence measurement of O₃. A flight within the marine boundary layer also demonstrated flux measurement capabilities, and we observed a mean O₃ deposition velocity of 0.029 ± 0.005 cm s⁻¹ to the ocean surface. The performance characteristics detailed below make ROZE a robust, versatile instrument for field measurements of O₃.

1 Introduction

In the troposphere, ozone (O₃) adversely affects air quality and acts as a greenhouse gas. Dry deposition to the Earth's terrestrial and oceanic surfaces represents a significant loss pathway for tropospheric O₃ (Young *et al.*, 2018) and thus influences tropospheric composition and O₃ pollution. Additionally, O₃ uptake through plant stomata leads to vegetation and crop damage (Ainsworth *et al.*, 2012; Mills *et al.*, 2018) and poor ecosystem health (Lombardozzi *et al.*, 2015), potentially amplifying the effects of O₃ on climate (Sitch *et al.*, 2007) and air quality (Sadiq *et al.*, 2017). Despite its role in the tropospheric O₃ budget, dry deposition velocities (v_d) of O₃ remain poorly constrained (Wesely and Hicks, 2000; Hardacre *et al.*, 2015). The observational records of terrestrial v_d (O₃) are limited in number and do not capture the full variability in O₃ deposition rates with land cover (Clifton *et al.*, 2020a). Furthermore, studies of O₃ deposition to the ocean (e.g., Kawa and Pearson, 1989; Faloon *et al.*, 2005; Helmig *et al.*, 2012; Novak *et al.*, 2020) report deposition velocities of ~0.01–0.05 cm s⁻¹, which are 1–2 orders of magnitude lower than typical terrestrial values. Observations from Helmig *et al.* (2012) and Novak *et al.* (2020) also suggest that O₃ deposition may vary with sea surface temperature. Global chemistry modeling frameworks that incorporate O₃ dry deposition (e.g., Bey *et al.*, 2001; Lamarque *et al.*, 2012) often apply fixed deposition rates to the ocean and heavily parameterized deposition schemes over land (Wesely, 1989). However, process-level representation of O₃ deposition improves agreement between modeled and observed surface O₃ concentrations (Clifton *et al.*, 2020b; Pound *et al.*, 2020). The range and variability in O₃ deposition rates thus motivates the need for further v_d (O₃) measurements to refine both atmospheric and land surface model predictions.



40 Measurements of vertical O₃ fluxes are typically accomplished via eddy covariance (EC) analysis. The EC technique demands fast
time-response, high-precision sensors to resolve the turbulence-driven variability in scalar concentrations. O₃ fluxes are therefore
measured using highly sensitive O₃ detection methods such as chemiluminescence (e.g., Bariteau *et al.*, 2010; Muller *et al.*, 2010)
and, more recently, chemical ionization mass spectrometry (CIMS) (Novak *et al.*, 2020). Chemiluminescence detectors employ
either nitric oxide (NO) gas or organic dyes, which generate photons on reaction with O₃. While these instruments exhibit good
sensitivity, they have practical drawbacks involving the use of toxic compressed gas cylinders and chemical dyes. Novak *et al.*
(2020) successfully demonstrated the use of oxygen anion CIMS to measure O₃ and its vertical fluxes with a detection limit of <
45 0.005 cm s⁻¹ over the ocean. To the best of our knowledge, ultraviolet (UV) absorption instruments have not previously been
utilized for O₃ flux measurements due to insufficient sensitivity (e.g., Gao *et al.*, 2012). However, advancements in incoherent
cavity-enhanced absorption spectroscopy (Fiedler *et al.*, 2003) facilitate the development of high-sensitivity sensors that are both
robust and compact. Furthermore, UV absorption has the advantage of providing direct detection of O₃ without the need for a
chemical titration source.

50

We report on the development of the NASA Rapid Ozone Experiment (ROZE), a cavity-enhanced UV absorption instrument for
the *in-situ* detection of O₃. The long optical pathlength and small cavity volume enable high precision measurements in short
averaging times, making ROZE suitable for O₃ flux measurements with the EC technique. The compact instrument design supports
integration aboard research aircraft for both tropospheric and stratospheric deployment. We describe the principle of operation
55 along with major instrument components and performance characteristics below. We also discuss the field performance of ROZE
and demonstrate its EC capabilities using aircraft observations of O₃ deposition to the ocean surface.

2 Principle of operation

Incoherent broadband cavity-enhanced absorption spectroscopy (IBBCEAS) is an established tool for the detection of trace gas
species (Fiedler *et al.*, 2003; Ball *et al.*, 2004; Washenfelder *et al.*, 2008) including O₃ (Darby *et al.*, 2012; Gomez and Rosen,
60 2013). IBBCEAS relies on a broadband, incoherent light source coupled to a high-finesse optical cavity. Typically, a multi-channel
detector resolves structured absorption features in the ultraviolet (UV) or visible spectral regions. IBBCEAS exploits the long
optical pathlength generated in the cavity to enhance sensitivity, comparable to other cavity-enhanced methods such as cavity
ringdown spectroscopy (CRDS). However, unlike CRDS, IBBCEAS uses a relatively inexpensive light source as compared to a
narrow linewidth laser. Furthermore, the incoherent light source relaxes the stringent requirements for cavity alignment that
65 accompany other cavity enhanced methods such as CRDS, enabling a more robust instrument configuration for field environments.

ROZE employs the IBBCEAS technique for high-sensitivity measurements of O₃. As illustrated in Figure 1, a light-emitting diode
(LED) in the UV ($\lambda_{\text{max}} = 265$ nm) is collimated and coupled into an optical cavity via high-reflectivity mirrors. Exiting light is
passed to a photomultiplier tube (PMT) detector through a series of collection and filter optics. Figure 2 depicts the normalized
70 detected LED intensity, which accounts for the LED spectral irradiance, the optical bandpass filter transmission, and the
wavelength dependent PMT response. The LED spectrum overlaps with the O₃ Hartley band, and any O₃ present in the sample cell
attenuates the light intensity received at the detector. The use of optical filters on the PMT precludes the need for wavelength
resolution from a grating spectrometer and simplifies data reduction. Section 3.1 provides further details on the optical system.



75 Attenuation of light intensity in an IBBCEAS cavity results from trace gas absorption as well as extinction due to the mirrors and Rayleigh scatter. Accounting for these additional losses, the Beer-Lambert absorption coefficient, α_{abs} , is related to the observed change in intensity transmitted through the cavity as follows (Washenfelder *et al.*, 2008):

$$\alpha_{abs} = \left(\frac{I_0 - I}{I}\right) \left(\frac{1 - R}{d} + \alpha_{Ray}\right) \quad (1)$$

Here, I_0 is light intensity in the absence of any absorbing species, I is the intensity attenuated due to absorption, R is the mirror reflectivity, d is the physical distance separating the cavity mirrors, and α_{Ray} is the extinction due to Rayleigh scatter, a non-negligible component in the UV. The term $(1 - R)/d$ gives the theoretical cavity loss, α_{cav} , and represents the inverse of the maximum effective pathlength, L_{eff} . In cavity-enhanced techniques, L_{eff} can be many orders of magnitude larger than d , resulting in high sensitivity to the absorbing species. Equation 1 can also be expressed as $\alpha_{abs} = N\sigma_{abs}$, where N is number density of the absorbing species and σ_{abs} is the absorption cross section. In principle, accurate trace gas measurements require calibration of the α_{cav} term, as well as knowledge of the Rayleigh and absorption cross sections in the detected spectral region. The data processing and calibration for ROZE will be discussed in Sections 3.4 and 4.1, respectively.

3 Instrument description

ROZE consists of three main subsystems housed in a compact 58 cm long x 44 cm wide x 18 cm high chassis, with a total instrument weight of 19 kg (Figure 3). The optical plate – a custom aluminum honeycomb panel supported by friction dampened spring vibration isolators – provides a stable platform for the optical components, consisting of the LED, sample cell, and PMT. The remaining subsystems include the flow handling and the data acquisition. Each major subsystem is described in greater detail below. ROZE operates at 24 V_{DC} with a low-profile AC-DC switching power supply (Vicor VI-LU3-IU) capable of running off 115 or 230 V_{AC} (47–440 Hz), which can be supplied directly from the aircraft. Power consumption is less than 200 W and typically ~100 W. Table 1 summarizes ROZE design and performance characteristics.

95 3.1 Optical components

3.1.1 LED assembly

A UV LED ($\lambda_{max} = 265$ nm, FWHM = 10 nm) (Thorlabs M265D2) is mounted to a custom heat sink and temperature controlled to 30 °C with a thermo-electric cooler (TE Technology CH-21-1.0-1.3; Wavelength Electronics PTC2.5K-CH). The LED output power is separately monitored by a photodiode (Marktech MTPD4400D-1.5) inserted into the edge of a lens tube that holds the LED. The LED assembly attaches to a custom cage mount system that also houses the associated optics, including an aspheric collimation lens ($f = 79$ mm, Thorlabs ASL10142M) and a beam expander (Thorlabs BE02-UVB) in reverse to shrink the collimated LED output. For compactness, the LED assembly and cage system are mounted parallel to the sample cell, and two mirrors (Thorlabs NB1-K04) direct the beam 180° into the cell.

3.1.2 Sample cell

105 The sample cell is manufactured from an aluminum alloy tube measuring 30 cm in length with a 1.2 cm inner diameter. The cell mirrors (Layertech 109561) have a reflectivity of $R > 99.7\%$ over the detected spectral range (Figure 2) and a 500 mm radius of curvature. The mirrors are held directly at the cell ends on face type o-ring seals using custom, non-adjustable mounts fastened to tube collars. The mirror positions are configured to maximize centricity. Two gas ports direct the sample flow into and out of the cell at right angles. The sample enters through a custom cylindrical diffuser, a ring with circumferential openings adjacent to the



110 cell mirrors, that nests within the cell tube orthogonal to the ports. The diffuser helps minimize noise due to Rayleigh scatter from
turbulence within the cell at high sample flow rates. A pressure transducer (Omega MMA015V10P4K1T4A6) measures the cell
pressure from a port near the cell center. The entire cell is thermally regulated to 35 °C using resistive heaters and a precision
heater control (Wavelength Electronic PTC2.5K-CH).

3.1.3 PMT assembly

115 A PMT (Hamamatsu H10720-113) operating in analog mode collects the light exiting the cell. Two optical bandpass filters
(Thorlabs FGUV5-UV, Semrock FF01-260/16) transmit the cell output to a collection lens ($f = 35$ mm, Thorlabs LA4052-UV),
which images the beam onto the PMT photocathode. A UV window (Thorlabs WG40530-UV) glued into a custom PEEK lens
tube adapter seals to the PMT face with a Viton gasket, creating a leak-tight package for low-pressure (high-altitude) operation.
The PMT is thermally stabilized to 35 °C in the same manner as the sample cell. The PMT signal is passed to an amplifier circuit
120 (Analog Devices EVAL-ADA4625-1ARDZ) before digitization by the data acquisition system described below.

3.2 Flow system

The ROZE flow system is designed to achieve rapid flushing of the detection cell as required for fast concentration measurements.
However, ROZE samples at ambient pressure to maximize sensitivity, necessitating high throughput with a minimal pressure
differential. ROZE utilizes a linear diaphragm pump (Thomas 6025SE-150113) that can achieve a flow rate of up to 18 standard
125 liters per minute (SLM) through the system. The pump speed can also be adjusted by varying the supply current and has three pre-
set speeds that can be changed by a switch on the chassis front panel. A flow meter (Honeywell AWM5104) located between the
cell exhaust and the pump monitors the sample flow in real time.

ROZE O₃ measurements also require knowledge of the reference intensity (I_0) as detailed in Equation 1. A 3-way solenoid valve
130 (NResearch TC648T032) switches between the sample line (ambient air from the aircraft inlet) and the zero port, which attaches
to an internal Carulite O₃ scrubber (2B Technologies) to produce O₃-free air. Periodic zeroing during operation captures long-term
drift in I_0 due to the LED output, PMT response, and changing environmental conditions. Typically, the instrument opens to the
O₃ scrubber for 10 seconds every 5 minutes.

135 ROZE uses fluorinated ethylene propylene (FEP) tubing both external and internal to the chassis upstream of the sample cell.
External to the chassis, the inlet details depend on the aircraft platform. ROZE has previously used the inlet detailed in Cazorla *et*
al. (2015) when flying on the NASA DC-8 aircraft. The instrument exhaust plumbs directly to an exhaust port near the rear of the
aircraft. To exclude dust and other particles from affecting the mirror reflectivity, a 2-micron pleated mesh filter (Swagelock)
affixes to the sample cell inlet port. More aggressive filtering can be achieved at the cost of reduced (< 18 SLM) flow rates but
140 may be necessary depending on the environment and if O₃ deposition measurements are not the primary goal.

3.3 Data acquisition

ROZE utilizes a CompactRIO (National Instruments cRIO-9030) that incorporates a real-time operating system and a Field
Programmable Gate Array (FPGA). The FPGA is configured for modulation of the LED and subsequent digitization of the PMT
signal. To improve measurement precision and remove background due to ambient light scatter, the FPGA modulates the LED at
145 1 kHz with a 90% duty cycle via an external LED driver (Wavelength Electronics FL591FL). A 16-bit Analog to Digital Converter
(ADC) digitizes the amplified PMT signal at a digitization rate of 100 kHz. This high rate enables us to average each LED ON and



OFF pulse amplitude. We then take the difference of the ON and OFF signals to remove background noise, both optical (i.e., stray light) and electronic. The 1 kHz differences are further averaged to 10 Hz and recorded. Other diagnostic housekeeping variables (e.g., sample flow, temperatures, LED power) are recorded at 1 Hz. Additionally, an analog output commands the 3-way valve to open to the zero line with a user-defined period and duration.

3.4 Data processing

In practice, the absorbance calculation for ROZE factors in the pressure difference between the sample and zero lines, as derived by Min *et al.* (2016):

$$\alpha_{O_3} = \left(\frac{I_z}{I} - 1\right) (\alpha_{cav} + \alpha_{Ray,Z}) + \Delta\alpha_{Ray} \quad (2)$$

Analogous to Equation 1, I_z is the intensity measured when sampling through the zero line (O₃-scrubbed air), I is the intensity when sampling ambient air, and $\Delta\alpha_{Ray} = \alpha_{Ray,Z} - \alpha_{Ray,S}$, where $\alpha_{Ray,Z}$ and $\alpha_{Ray,S}$ give the Rayleigh extinction ($\alpha_{Ray} = N_{air}\sigma_{Ray}$) of the zero and the sample respectively. The O₃ number density can then be determined as $\alpha_{O_3} = N_{O_3}\sigma_{O_3}$. The Rayleigh scattering (Bucholtz, 1995) and O₃ absorption (Serdyuchenko *et al.*, 2014) cross sections are calculated as the weighted average over the collected spectral range (Figure 2). Using known cross sections and a calibrated α_{cav} (inverse effective pathlength), the observed change in intensity yields a direct measure of the O₃ concentration.

4 Performance

4.1 Sensitivity and calibration

The effective pathlength of the ROZE optical cavity determines the instrument sensitivity to O₃ (i.e., the attenuation in intensity per unit O₃). The cavity extinction, and thus the effective pathlength, are dictated by the mirror reflectivity as described above but require independent calibration. Calibration can be accomplished via standard addition of O₃ or Rayleigh attenuation (in the absence of absorbing species) at varied sample pressures. The former method relies on commercially available O₃ generators or sensors for verification, which lack the required accuracy and may drift over time. In contrast, the Rayleigh calibration provides a convenient and straightforward alternative. Both methods are described below.

Figure 4a depicts the ROZE calibration using known concentrations of O₃. A commercial O₃ source (2B Technologies 306) generated known amounts of O₃, with the zero O₃ addition serving as the I_z baseline. Per Equation 2, the slope of the observed attenuation ($dI = I_z/I - 1$) as a function of O₃ number density is proportional to the remaining extinction terms ($\alpha_{cav} + \alpha_{Ray}$). Solving for α_{cav} using the O₃ cross section and the calculated Rayleigh extinction, the calibration yields an effective pathlength of $L_{eff} = 108 \pm 6$ m. The alternate calibration uses the Rayleigh extinction in zero air over a range of cell pressures (Figure 4b). In the absence of absorbing species, an expression for α_{cav} can be derived following the approach in Washenfelder *et al.* (2008) as:

$$\alpha_{Ray} = \left(\frac{I_0}{I} - 1\right) \alpha_{cav} \quad (3)$$

I_0 represents the intensity at vacuum, which can be extrapolated from a linear fit of counts as a function of cell pressure. The slope of the observed change in intensity with number density therefore yields a direct measure of the cavity extinction, resulting in an effective pathlength of 104 ± 4 m. The two methods agree to within fit uncertainties, and we use L_{eff} as determined by the Rayleigh calibration for subsequent calculations.



4.2 Precision and accuracy

The major contributions to instrument noise include PMT electrical noise and differential scatter or absorption due to non-uniform flow within the sample cell at high flow rates. The flow diffuser (see Section 3.1.2) effectively reduces the flow noise, while decreasing the gain on the PMT amplifier circuit minimizes the PMT electrical noise. The ROZE precision can be determined from the continuous sampling of zero air at a constant pressure. Figure 5 depicts a 1σ Allan deviation plot for ROZE (in pptv O₃ equivalents) as calculated from optical extinction measurements of zero air acquired over 1.5 hours at 944 mbar. For short integration times (< 10 s), a fit of the data gives a $\tau^{-0.47}$ decay, indicating the Allan deviation closely follows the square root of the averaging time ($\tau^{-1/2}$) as expected for white noise. At the native 0.1 s sampling rate, the 1σ precision for O₃ is 80 pptv and reduces to 31 pptv with 1 s averaging. For the given cell pressure and a temperature of 35 °C, this translates to a 1σ precision of 6.7×10^8 molecules cm⁻³ (1 s average) of O₃.

The absolute accuracy of the ROZE measurement depends on uncertainties in the literature-reported values of the O₃ and Rayleigh cross sections, the measured cell temperature and pressure, and the calibrated cavity extinction. The reported O₃ absorption cross section has an uncertainty of 2% (Gorshchev *et al.*, 2014), and we estimate an upper uncertainty of 3% for the Rayleigh scattering cross section (Bucholtz, 1995). The cell pressure and temperature are accurate to within 0.2% and 0.5% respectively, and the calibrated cavity extinction has an additional 4% slope uncertainty from the linear fit. These errors propagate through Equation 2 to yield a total measurement uncertainty of 6.2% in the O₃ number density.

4.3 Response time

The flush time of the sample cell limits the true instrument response time despite the 10 Hz data acquisition rate. A rapid flush rate is critical for high spatial resolution measurements from a fast-moving platform. Additionally, fast concentration measurements are required for sampling of turbulent eddies for airborne EC, and the necessary time response scales with aircraft speed. Response times of 10 Hz are typically considered sufficient for ground-based EC (Aubinet *et al.*, 2012), while for airborne EC, a response times of 1–5 Hz are typically sufficient due to larger eddy scales at altitude (Wolfe *et al.*, 2018). Figure 6a shows the instantaneous instrument response to a series of 10 ms pulses of O₃ injected into a zero-air carrier flow using a fast switching valve (The Lee Company, IEP series). During this experiment, the pump maintained a sample flow rate of 18 SLM. A series of exponential decay fits for several O₃ pulses yields an e -folding time constant of $\tau_r = 50 \pm 4$ ms (Figure 6b). The time constant corresponds to a 3 e -fold flush rate of 9.5 Hz.

5 Field demonstration

ROZE can be operated on both low- and high-altitude aircraft platforms. Though ROZE has not yet flown on a high-altitude unpressurized aircraft (such as the NASA ER-2), laboratory experiments in a thermal vacuum chamber have demonstrated no loss of performance down to a pressure and temperature of 50 mbar and 250 K (results not shown).

In summer 2019, ROZE flew aboard the NASA DC-8 for the Fire Influence on Regional to Global Environments Experiment, Air Quality (FIREX-AQ) campaign over the Central and Northwest United States. Campaign flights targeted smoke plumes from forest wildfires and agricultural burns. The instrument operated as described above, with the addition of an inline particle filter (Balston 9922-05-DQ) to protect the cavity mirrors from fine particulates in the smoke. In fresh, concentrated smoke plumes, UV-active species such as SO₂ and aromatic hydrocarbons can give rise to positive artifacts in the O₃ absorption measurement (Birks,



2015). This is a drawback to the UV absorption measurement, which can be affected by both absorbing and scattering molecules. However, such UV-active absorbers are generally not abundant enough in the background atmosphere to be of concern. The
220 FIREX-AQ ROZE data are therefore quality filtered to remove points sampled within dense smoke plumes using observed formaldehyde mixing ratios above 5 ppbv. Below, we detail comparisons of ROZE against an established O₃ measurement. Additionally, level flight legs in the marine boundary layer during a flight over the ocean provide an initial demonstration of O₃ vertical flux measurements.

5.1 Validation against chemiluminescence

225 The DC-8 FIREX-AQ payload included the NOAA Nitrogen Oxides and Ozone (NOyO₃) instrument, a well-established O₃ measurement using the chemiluminescence technique (Ryerson *et al.*, 2000; Bourgeois *et al.*, 2020). ROZE operated simultaneously with the NOyO₃ instrument during several flights. Figure 7 shows a comparison of ROZE and NOyO₃ data for the July 30, 2019 flight over the Northwestern United States. During this flight, no fresh smoke plumes were sampled, and no filtering of the ROZE data was necessary. Figure 7a depicts a ~25 min subset of the full timeseries to illustrate the ROZE instrument
230 precision. Both measurements (averaged to 1 s) track the dynamic features in O₃ mixing ratios well. The cross plot for the full flight (Figure 7b) demonstrates strong agreement between the two measurements, with a slope of 0.98 ± 0.01 and an intercept of 0.17 ± 0.02 ppbv O₃ ($r_2 = 0.99$). Comparisons for 15 flights from the campaign indicate a range in slopes of 0.96–1.04, consistent with the measurement uncertainty.

5.2 Ozone flux measurements

235 5.2.1 Eddy covariance flux

The vertical flux of O₃ can be directly quantified using the eddy covariance (EC) technique. EC defines the flux (F) as the time or spatially averaged covariances in the vertical wind speed (w) and the scalar species of interest (in this case the O₃ mixing ratio X_{O_3}):

$$F_{O_3} = \langle w'X_{O_3}' \rangle \quad (4)$$

240 In the equation above, the primes denote instantaneous deviations from the mean value, and the brackets indicate an average over a prescribed interval as discussed below. Since deposition dominates transfer across the air-surface interface, the O₃ flux can instead be expressed as a transfer rate or deposition velocity (v_d):

$$v_d = -\frac{F_{O_3}}{\bar{X}_{O_3}} \quad (5)$$

245 Here, the overbar indicates the mean O₃ mixing ratio over the averaging period. The deposition velocity, in units of cm s⁻¹, yields a normalized metric of the deposition efficiency and incorporates both chemical and physical transfer processes.

During the FIREX-AQ campaign, the flight on July 17, 2019 contained a level segment within the turbulent marine boundary layer suitable for EC. The flux transects were located over the Pacific Ocean, ~200 miles southwest of the Los Angeles Basin. To quantify O₃ deposition, the Meteorological Measurement System (MMS) instrument provided 3-D wind vector data (Chan *et al.*,
250 1998), which were used in conjunction with ROZE O₃ measurements. A 1-D coordinate rotation was applied to the wind vector to force the mean vertical wind to zero, and the native 20 Hz MMS data was averaged to the ROZE 10 Hz time base. Note that the additional particle filter reduced the ROZE sample flow to 11.3 SLM, and we estimate the time constant from the decay of zero-O₃ additions as $\tau_r = 90$ ms (5.5 Hz $1/3e$ flush rate). We also use 20 Hz water vapor measurements from the open path Diode Laser Hygrometer (DLH) (Diskin *et al.*, 2002) as a benchmark for the flux performance. 20 Hz DLH data were averaged to the ROZE



255 time base and used to apply a moist-to-dry air correction for raw O₃ observations, negating the need for density corrections to the
calculated flux (Webb *et al.*, 1980). This density correction reduces the O₃ flux by ~6%. For the EC calculations, we selected two
~50 km transects with consistent aircraft heading, stationary flow, and level altitude (~170 m). Scalar data processing included
detrrending the scalar mixing ratios by subtracting a 20 second running mean and synchronizing the data with the vertical winds.

260 5.2.2 Spectral analysis

Spectral analysis aids in decomposing the contributions of eddies at different scales (frequencies) to the overall signal and provides
a quality assessment of the ROZE flux measurements. Figure 8 displays the lag-covariance, power spectrum, and co-spectrum for
O₃ and vertical wind fluctuations generated using fast Fourier transforms (FFTs) for a single transect. The spectra for water vapor
are also displayed for comparison. The lagged cross-cross covariance functions (Figure 8a) demonstrate defined peaks at lags of <
265 0.5 s, with the peak non-normalized covariance yielding a measure of the flux. Dividing out the background O₃ mixing ratio of 29
ppbv, we find a mean deposition velocity of 0.029 cm s⁻¹ for the two transects. The power spectra in Figure 8b show that vertical
winds follow the theoretical $f^{-5/3}$ decay expected in the inertial subrange (Kaimal *et al.*, 1972). The slope for the O₃ power
spectrum initially follows the same decay but flattens at ~1 Hz, indicating that the turbulence-driven variability in O₃ approaches
the ROZE precision limit in higher-frequency eddies. However, the normalized frequency-weighted co-spectral power of w' with
270 X_{O_3}' (Figure 8c, solid lines) show that flux carrying eddies below ~0.6 Hz dominate the total signal. The ogive, the cumulative
integral of the co-spectrum (Fig. 8c, dashed lines) further indicates that 99% of flux carrying eddies occur at frequencies below ~4
Hz. These results demonstrate the adequate ROZE time response for airborne EC.

5.2.3 Flux uncertainty

Detailed methods to quantify flux errors for airborne EC can be found elsewhere (Lenschow *et al.*, 1994; Langford *et al.*, 2015;
275 Wolfe *et al.*, 2018). Here, we aim to quantify the random and systematic flux errors that reflect the overall instrument performance.
We use the empirical formulation of Finkelstein and Sims (2001) to estimate the total random error (RE_{TOT}) as the variance of the
scalar-wind covariance. In this approach, the RE_{TOT} is determined using auto- and cross-correlation functions (as in Figure 8a)
over lag times that are sufficient to capture the timescale of the correlation (here ~10 s). Averaging over the flux legs yields a
RE_{TOT} of 0.005 cm s⁻¹. RE_{TOT} encompasses both instrument noise as well as error from the random sampling of turbulence. To
280 isolate the RE component due solely to instrument noise (RE_{noise}), we follow the approach of Mauder *et al.* (2013). In this method,
the standard deviation of the instrument noise is derived from the scalar auto-covariance and then propagated to determine its
contribution to the to the cross-covariance uncertainty. Note that RE_{noise} still depends on the turbulence regime and therefore varies
with atmospheric conditions. We calculate RE_{noise} to be 0.0015 cm s⁻¹ averaging over the two flux transects. These results indicate
that instrument noise constitutes ~30% of the total random error.

285 Additionally, the instrument time response can lead to systematic flux errors as a consequence of under sampling contributions
from high-frequency eddies. We determine the systematic error due to the instrument response time (SE_{RT}) following the Horst
(1997) model, whereby the attenuation in the measured signal can be expressed as a co-spectral transfer function based on the
characteristic instrument response time. Using the ROZE response time of $\tau_r = 90$ ms, we determine SE_{RT} as < 2%, indicating
290 minimal attenuation in the measured flux signal.



6 Summary and conclusions

The NASA ROZE instrument provides high sensitivity, fast time response measurements of O₃ via broadband cavity-enhanced UV absorption. The compact, robust instrument package is adaptable to diverse field environments, including low- and high-altitude aircraft platforms. ROZE currently achieves a 1σ precision of ~ 30 pptv s⁻¹ and an overall accuracy of 6.2%. ROZE was successfully integrated aboard the NASA DC-8 aircraft, and the field performance compares favorably with an independent O₃ measurement to within ROZE uncertainty. The maximum observed time response for laboratory tests was 50 ms, with additional filtering during aircraft operation slowing the time response to 90 ms. The instrument precision and time response make ROZE particularly well suited for vertical O₃ flux measurements using eddy covariance analysis. ROZE has measured O₃ deposition velocities of 0.029 ± 0.005 cm s⁻¹ to the ocean surface, with minimal (< 2%) response-time attenuation in the flux signal. The demonstrated performance of ROZE makes the instrument an ideal and versatile option for field measurements of both O₃ concentrations and fluxes.

Data availability

The FIREX-AQ data for O₃ (ROZE and NOyO₃), water vapor (DLH), formaldehyde (ISAF), and 3-D winds (MMS) are publicly available at <https://www-air.larc.nasa.gov/missions/firex-aq/>.

Acknowledgements

This work was supported by the NASA Internal Research and Development (IRAD) program, the NASA Upper Atmosphere Research Program, and the NASA Tropospheric Chemistry Program. The aircraft flight opportunity was provided by the NASA/NOAA FIREX-AQ project and the NASA Student Airborne Research Program (SARP). We would like to acknowledge the DLH instrument team (Glenn Diskin, et al.) for the water vapor measurements used in the eddy covariance analysis. We would additionally like to thank Jason St. Clair and Glenn Wolfe for helpful comments on the manuscript.

References

- Ainsworth, E. A. *et al.* (2012) ‘The Effects of Tropospheric Ozone on Net Primary Productivity and Implications for Climate Change’, *Annual Review of Plant Biology*, 63(1), pp. 637–661. doi: 10.1146/annurev-arplant-042110-103829.
- Aubinet, M., Vesala, T. and Papale, D. (eds) (2012) *Eddy Covariance, Eddy Covariance: A Practical Guide to Measurement and Data Analysis*. Dordrecht: Springer Science+Business Media. doi: 10.1007/978-94-007-2351-1.
- Ball, S. M., Langridge, J. M. and Jones, R. L. (2004) ‘Broadband cavity enhanced absorption spectroscopy using light emitting diodes’, *Chemical Physics Letters*, 398(1–3), pp. 68–74. doi: 10.1016/j.cplett.2004.08.144.
- Bariteau, L. *et al.* (2010) ‘Determination of oceanic ozone deposition by ship-borne eddy covariance flux measurements’, *Atmospheric Measurement Techniques*, 3(2), pp. 441–455. doi: 10.5194/amt-3-441-2010.
- Bey, I. *et al.* (2001) ‘Global modeling of tropospheric chemistry with assimilated meteorology: Model description and evaluation’, *Journal of Geophysical Research: Atmospheres*, 106(D19), pp. 23073–23095. doi: 10.1029/2001JD000807.
- Birks, J. (2015) UV-Absorbing Interferences in Ozone Monitors.
- Bourgeois, I. *et al.* (2020) ‘Global-scale distribution of ozone in the remote troposphere from ATom and HIPPO airborne field missions’, *Atmospheric Chemistry and Physics Discussions*, pp. 1–52. doi: 10.5194/acp-2020-315.
- Bucholtz, A. (1995) ‘Rayleigh-scattering calculations for the terrestrial atmosphere’, *Applied Optics*, 34(15), p. 2765. doi: 10.1364/AO.34.002765.



- Cazorla, M. *et al.* (2015) ‘A new airborne laser-induced fluorescence instrument for in situ detection of formaldehyde throughout the troposphere and lower stratosphere’, *Atmospheric Measurement Techniques*, 8(2), pp. 541–552. doi: 10.5194/amt-8-541-2015.
- 330 Chan, K. R. *et al.* (1998) ‘Turbulence measurements by the DC-8 Meteorological Measurement System’, *Geophysical Research Letters*, 25(9), pp. 1355–1358. doi: 10.1029/97GL03590.
- Clifton, Olivia E. *et al.* (2020) ‘Dry Deposition of Ozone Over Land: Processes, Measurement, and Modeling’, *Reviews of Geophysics*, 58(1). doi: 10.1029/2019RG000670.
- Clifton, O. E. *et al.* (2020) ‘Influence of Dynamic Ozone Dry Deposition on Ozone Pollution’, *Journal of Geophysical Research: Atmospheres*, p. e2020JD032398. doi: 10.1029/2020jd032398.
- 335 Darby, S. B., Smith, P. D. and Venables, D. S. (2012) ‘Cavity-enhanced absorption using an atomic line source: application to deep-UV measurements’, *The Analyst*, 137(10), p. 2318. doi: 10.1039/c2an35149h.
- Diskin, G. S. *et al.* (2002) ‘Open-path airborne tunable diode laser hygrometer’, in Fried, A. (ed.) *Proc SPIE, Diode Lasers and Applications in Atmospheric Sensing*, p. 196. doi: 10.1117/12.453736.
- 340 Faloon, I. *et al.* (2005) ‘Observations of Entrainment in Eastern Pacific Marine Stratocumulus Using Three Conserved Scalars’, *Journal of the Atmospheric Sciences*, 62(9), pp. 3268–3285. doi: 10.1175/JAS3541.1.
- Fiedler, S. E., Hese, A. and Ruth, A. A. (2003) ‘Incoherent broad-band cavity-enhanced absorption spectroscopy’, *Chemical Physics Letters*, 371(3–4), pp. 284–294. doi: 10.1016/S0009-2614(03)00263-X.
- Gao, R. S. *et al.* (2012) ‘A compact, fast UV photometer for measurement of ozone from research aircraft’, *Atmospheric Measurement Techniques*, 5(9), pp. 2201–2210. doi: 10.5194/amt-5-2201-2012.
- 345 Gomez, A. L. and Rosen, E. P. (2013) ‘Fast response cavity enhanced ozone monitor’, *Atmospheric Measurement Techniques*, 6(2), pp. 487–494. doi: 10.5194/amt-6-487-2013.
- Gorshelev, V. *et al.* (2014) ‘High spectral resolution ozone absorption cross-sections – Part 1: Measurements, data analysis and comparison with previous measurements around 293 K’, *Atmospheric Measurement Techniques*, 7(2), pp. 609–624. doi: 10.5194/amt-7-609-2014.
- 350 Hardacre, C., Wild, O. and Emberson, L. (2015) ‘An evaluation of ozone dry deposition in global scale chemistry climate models’, *Atmospheric Chemistry and Physics*, 15(11), pp. 6419–6436. doi: 10.5194/acp-15-6419-2015.
- Helmig, D. *et al.* (2012) ‘Atmosphere-ocean ozone fluxes during the TexAQs 2006, STRATUS 2006, GOMECC 2007, GasEx 2008, and AMMA 2008 cruises’, *Journal of Geophysical Research: Atmospheres*, 117(D4). doi: 10.1029/2011JD015955.
- 355 Horst, T. W. (1997) ‘A simple formula for the attenuation of eddy fluxes measured with first-order-response scalar sensors’, *Boundary-Layer Meteorology*, 82(2), pp. 219–233. doi: 10.1023/A:1000229130034.
- Kaimal, J. C. *et al.* (1972) ‘Spectral characteristics of surface-layer turbulence’, *Quarterly Journal of the Royal Meteorological Society*, 98(417), pp. 563–589. doi: 10.1002/qj.49709841707.
- Kawa, S. R. and Pearson, R. (1989) ‘Ozone budgets from the dynamics and chemistry of marine stratocumulus experiment’, *Journal of Geophysical Research*, 94(D7), p. 9809. doi: 10.1029/JD094iD07p09809.
- 360 Lamarque, J.-F. *et al.* (2012) ‘CAM-chem: description and evaluation of interactive atmospheric chemistry in the Community Earth System Model’, *Geoscientific Model Development*, 5(2), pp. 369–411. doi: 10.5194/gmd-5-369-2012.
- Langford, B. *et al.* (2015) ‘Eddy-covariance data with low signal-to-noise ratio: time-lag determination, uncertainties and limit of detection’, *Atmospheric Measurement Techniques*, 8(10), pp. 4197–4213. doi: 10.5194/amt-8-4197-2015.
- 365 Lenschow, D. H., Mann, J. and Kristensen, L. (1994) ‘How Long Is Long Enough When Measuring Fluxes and Other Turbulence Statistics?’, *Journal of Atmospheric and Oceanic Technology*, 11(3), pp. 661–673. doi: 10.1175/1520-0426.
- Lombardozi, D. *et al.* (2015) ‘The influence of chronic ozone exposure on global carbon and water cycles’, *Journal of Climate*, 28(1), pp. 292–305. doi: 10.1175/JCLI-D-14-00223.1.
- Mauder, M. *et al.* (2013) ‘A strategy for quality and uncertainty assessment of long-term eddy-covariance measurements’, *Agricultural and Forest Meteorology*, 169, pp. 122–135. doi: 10.1016/j.agrformet.2012.09.006.
- 370 Mills, G. *et al.* (2018) ‘Ozone pollution will compromise efforts to increase global wheat production’, *Global Change Biology*, 24(8), pp. 3560–3574. doi: 10.1111/gcb.14157.
- Min, K.-E. *et al.* (2016) ‘A broadband cavity enhanced absorption spectrometer for aircraft measurements of glyoxal, methylglyoxal, nitrous acid, nitrogen dioxide, and water vapor’, *Atmospheric Measurement Techniques*, 9(2), pp. 423–440. doi: 10.5194/amt-9-423-2016.



- 375 Muller, J. B. A. *et al.* (2010) ‘Sources of uncertainty in eddy covariance ozone flux measurements made by dry chemiluminescence fast response analysers’, *Atmospheric Measurement Techniques*, 3(1), pp. 163–176. doi: 10.5194/amt-3-163-2010.
- Novak, G. A., Vermeuel, M. P. and Bertram, T. H. (2020) ‘Simultaneous detection of ozone and nitrogen dioxide by oxygen anion chemical ionization mass spectrometry: a fast-time-response sensor suitable for eddy covariance measurements’, *Atmospheric Measurement Techniques*, 13(4), pp. 1887–1907. doi: 10.5194/amt-13-1887-2020.
- 380 Pound, R. J. *et al.* (2020) ‘Influences of oceanic ozone deposition on tropospheric photochemistry’, *Atmospheric Chemistry and Physics*, 20(7), pp. 4227–4239. doi: 10.5194/acp-20-4227-2020.
- Ryerson, T. B., Williams, E. J. and Fehsenfeld, F. C. (2000) ‘An efficient photolysis system for fast-response NO₂ measurements’, *Journal of Geophysical Research: Atmospheres*, 105(D21), pp. 26447–26461. doi: 10.1029/2000JD900389.
- 385 Sadiq, M. *et al.* (2017) ‘Effects of ozone–vegetation coupling on surface ozone air quality via biogeochemical and meteorological feedbacks’, *Atmospheric Chemistry and Physics*, 17(4), pp. 3055–3066. doi: 10.5194/acp-17-3055-2017.
- Serduchenko, A. *et al.* (2014) ‘High spectral resolution ozone absorption cross-sections – Part 2: Temperature dependence’, *Atmospheric Measurement Techniques*, 7(2), pp. 625–636. doi: 10.5194/amt-7-625-2014.
- Sitch, S. *et al.* (2007) ‘Indirect radiative forcing of climate change through ozone effects on the land-carbon sink’, *Nature*, 448(7155), pp. 791–794. doi: 10.1038/nature06059.
- 390 Washenfelder, R. A. *et al.* (2008) ‘Measurement of glyoxal using an incoherent broadband cavity enhanced absorption spectrometer’, *Atmospheric Chemistry and Physics*, 8(24), pp. 7779–7793. doi: 10.5194/acp-8-7779-2008.
- Webb, E. K., Pearman, G. I. and Leuning, R. (1980) ‘Correction of flux measurements for density effects due to heat and water vapour transfer’, *Quarterly Journal of the Royal Meteorological Society*, 106(447), pp. 85–100. doi: 10.1002/qj.49710644707.
- 395 Wesely, M. L. (1989) ‘Parameterization of surface resistances to gaseous dry deposition in regional-scale numerical models’, *Atmospheric Environment (1967)*, 23(6), pp. 1293–1304. doi: 10.1016/0004-6981(89)90153-4.
- Wesely, M. L. and Hicks, B. B. (2000) ‘A review of the current status of knowledge on dry deposition’, *Atmospheric Environment*, 34(12–14), pp. 2261–2282. doi: 10.1016/S1352-2310(99)00467-7.
- Wolfe, G. M. *et al.* (2018) ‘The NASA Carbon Airborne Flux Experiment (CARAFE): instrumentation and methodology’, *Atmospheric Measurement Techniques*, 11(3), pp. 1757–1776. doi: 10.5194/amt-11-1757-2018.
- 400 Young, P. J. *et al.* (2018) ‘Tropospheric Ozone Assessment Report: Assessment of global-scale model performance for global and regional ozone distributions, variability, and trends’, *Elem Sci Anth*, 6(1), p. 10. doi: 10.1525/elementa.265.

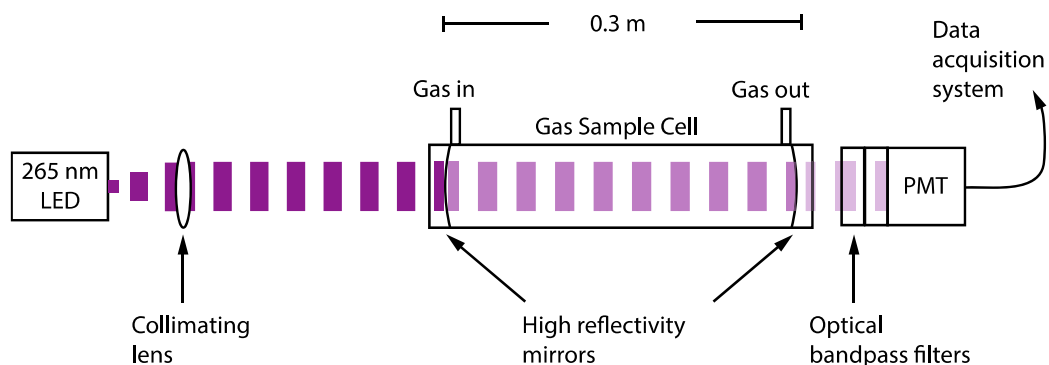


Table 1: Summary of ROZE performance capabilities.

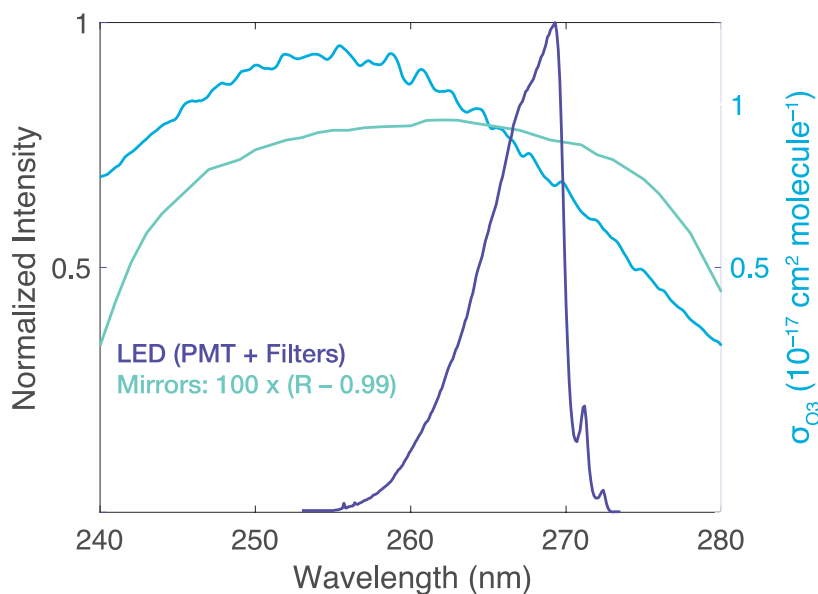
Specification	Value
Size	58 x 44 x 18 cm
Weight	19 kg
Power	< 200 W
Data rate	10 Hz
Precision (1σ , 1Hz)	6.7×10^8 molec. cm^{-3}
Accuracy	6.2%
Time response	50 ms



405

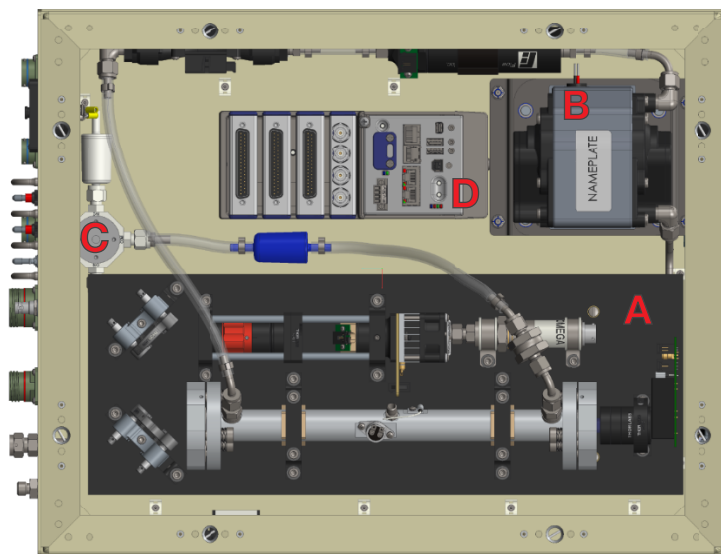


410 **Figure 1: Incoherent broadband cavity enhanced detection technique for O₃. A LED at 265 nm is collimated and coupled into the detection cell via high reflectivity mirrors ($R > 99.7\%$), creating a long optical pathlength. The light attenuated by the sample is then detected using a photomultiplier tube (PMT) operated in analog mode. The sample enters and exits the cell orthogonal to the beam propagation.**

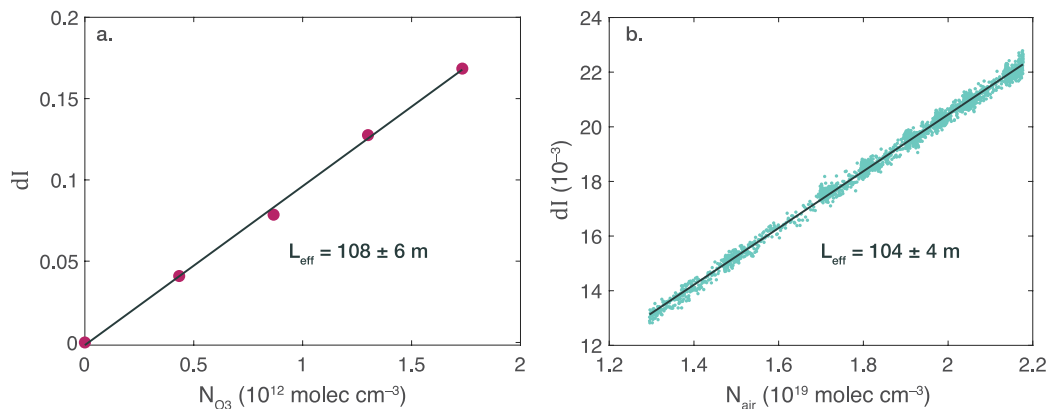


415 **Figure 2: LED spectrum, mirror reflectivity, and O₃ absorption cross section: The LED ($\lambda_{\max} = 265$ nm, FWHM = 10 nm) spectrum was measured using a grating spectrometer (0.1 nm resolution) with the instrument PMT and associated detector optics. The mirror curve depicts $100 \times [R - 0.99]$, where R is the reflectivity, over a range of wavelengths. The right axis shows the absorption cross section for the O₃ Hartley band. O₃ and Rayleigh cross sections were determined as the weighted average with the normalized intensity of the LED and PMT detector optics.**

420



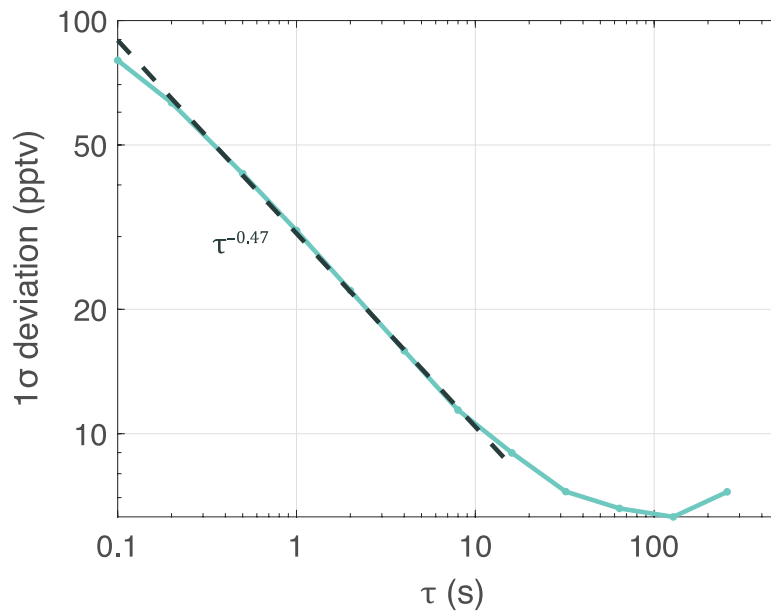
425 **Figure 3: A top view of the ROZE instrument chassis. Major components include A) the optical plate, which consists of the LED assembly, associated optics, the optical cell, and PMT detector; B) The diaphragm pump which can pull up to ~18 SLM through the flow system; C) The 3-way valve which switches between the sample line and air scrubbed of O₃ using a Carulite filter; and D) The data acquisition system.**



430

435

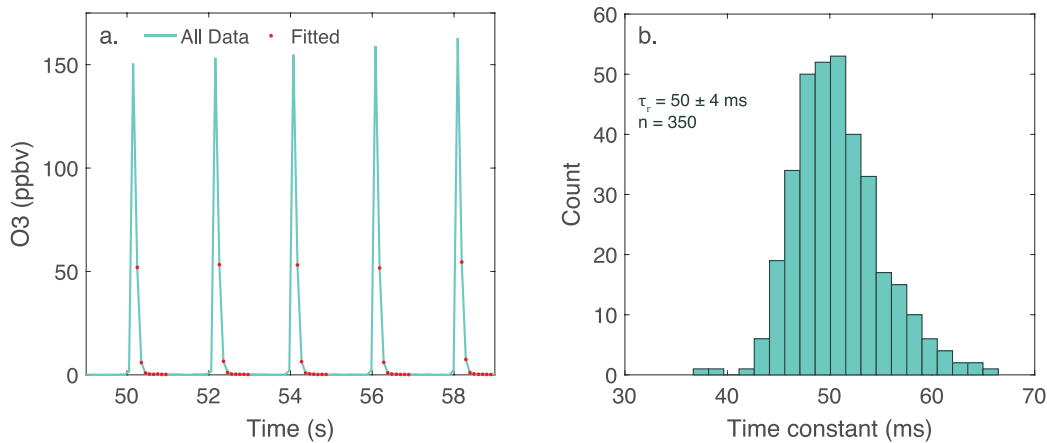
Figure 4: ROZE calibration: a) The effective pathlength (L_{eff}) as determined by attenuation (dI) due to known additions of O_3 from a commercial ozone-generator. The slope yields the effective pathlength as determined from Equation 1 in the text using the known O_3 absorption cross section; b) Attenuation due to Rayleigh scatter over a range of cell pressures. The slope of attenuation as a function of number density gives the pathlength using the known Rayleigh scattering cross section for zero air. The pathlength derived from both calibrations agrees to within the fit uncertainty.



440

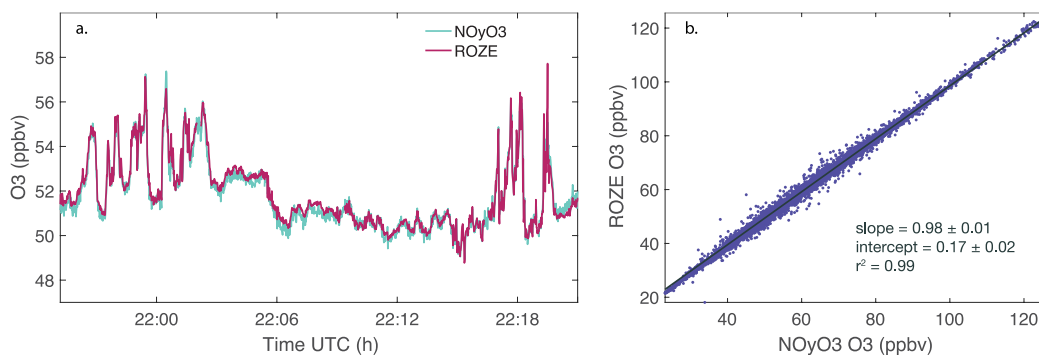
Figure 5: Allan deviation plot for 1.5 hr of sampling zero air at constant pressure (944 mbar). The 1σ precision is expressed in pptv equivalents of O_3 as a function of the integration time τ . The curve demonstrates a precision of 31 pptv in a 1 s integration time. The dashed line shows a $\tau^{-0.47}$ decay for short integration times (< 10 s), comparable to the $\tau^{-1/2}$ decay expected for white noise.

445

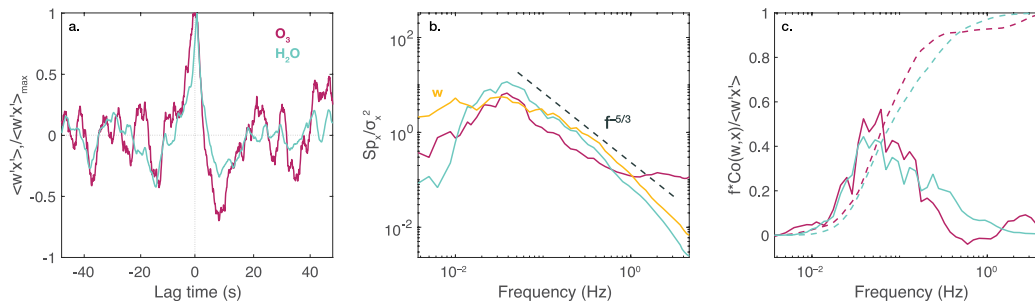


450 **Figure 6: ROZE time response: a) Ozone was injected into the flow system via a pulsed valve at 2-second intervals with a**
sample flow of 18 SLM. Individual pulses were fit to an exponential decay using the selected data points in red; b)
Histogram of time constants for all 350 pulses. The e -folding decay time of 50 ± 4 ms corresponds to a $(1/3e)$ flush rate of
9.5 Hz.

455



460 **Figure 7: ROZE and NO_yO₃ measurements of O₃ from a FIREX-AQ flight on July 30, 2019 over the Northwestern US: a) Timeseries of ROZE and NO_yO₃ data (averaged to 1 s); b) Scatter plot of ROZE and NO_yO₃ O₃ measurements from the full flight. A linear fit to the data yields a slope of $0.98 \pm .01$ and an intercept of 0.17 ± 0.02 ppbv.**



465

Figure 8: Example spectra from a 50 km flux leg at 170 m altitude during the July 17, 2019 flight over the Pacific Ocean:
a) Vertical wind-scalar (w and x respectively) cross covariance functions normalized by the maximum covariance for O_3 and water vapor; **b)** Power spectra normalized to total variance for w , O_3 , and H_2O . The dashed line represents the $f^{-5/3}$ theoretical decay for the inertial subrange; **c)** Solid lines depict co-spectral power (frequency-multiplied and covariance-normalized) of O_3 and H_2O with vertical wind. Dashed lines depict the respective ogives (cumulative integrals).

470